Design and Performance of the Monopulse Pointing System of the DSN 34-Meter Beam-Waveguide Antennas

M. A. Gudim,[1] W. Gawronski,[1] W. J. Hurd,[2] P. R. Brown,[1] and D. M. Strain[3]

This article describes the design, analysis, and performance prediction of a monopulse pointing system in a 34-m beam-waveguide antenna of the Deep Space Network (DSN). While the basic concept of monopulse pointing is not new, its application in the DSN is novel in two ways: first, the large antenna structure made necessary by the extremely weak signal environment; and second, the use of the single monopulse feed at 31.8 to 32.3 GHz (Ka-band) frequencies. The conventional aircraft radar application has a higher signal-to-noise ratio (SNR) with a fast, hostile tracking scenario. The DSN application requires precise antenna pointing to minimize pointing loss, maximize amplitude stability, and track very low-SNR signals from a very distant spacecraft with a well-predicted trajectory. The combination of the large antenna size, the low SNR, and the precise pointing requirements makes the monopulse implementation in the DSN a challenging task.

I. Introduction

Traditionally, the DSN has employed the conical scanning (CONSCAN) algorithm for pointing the antennas at 2.2 to 2.305 GHz (S-band) and 8.2 to 8.6 GHz (X-band). In CONSCAN, the pointing error is estimated by moving the antenna in a circle with respect to the best estimate of the spacecraft location. The received power detected on this circle is used to generate a new best estimate of the spacecraft location. Nominally, the circle chosen is such that the detected power is 0.1 dB less than the peak of the antenna beam. In the beam-waveguide antennas, the 0.1-dB beam widths are 22 mdeg at S-band, 5.9 mdeg at X-Band, and 1.5 mdeg at 31.8 to 32.3 GHz (Ka-band). At S- and X-band frequencies, a typical jitter of 1 mdeg in the antenna pointing (under favorable environmental conditions with no wind) does not result in significant fluctuations in detected power levels. At Ka-band, the same jitter causes significant fluctuations in the detected power levels—not acceptable for radio science application. For this reason, it became necessary to adopt a new technique that allows the antenna to be pointed directly at the spacecraft. An additional advantage is a 0.1-dB gain in signal by not having to point away from the spacecraft.

The selected monopulse pointing method employs a single monopulse feedhorn [1]. In this algorithm, the pointing error is estimated from two RF signals generated by the monopulse feedhorn. One signal

[1] Communications Ground Systems Section.

[2] TMOD Plans and Commitments Program Office.

[3] Communications Ground Systems Section, Planning Research Corporation.

propagates in a TE_{11} circular-waveguide mode, and the other propagates in a TE_{21} circular-waveguide mode. These signals are uniquely related in amplitude and phase as a function of the antenna-pointing error. The single monopulse feed design allows direct pointing at the target at all times, allowing for the spacecraft to be tracked at the peak of the antenna pattern. In addition, use of a single horn makes calibration easier than for the traditional monopulse configuration with three to five feedhorns. This article describes the design and analysis and provides performance predictions for monopulse systems implemented in the DSN 34-m-diameter beam-waveguide (BWG) antennas.

II. Key Design Issues

For implementation of a monopulse system in the DSN 34-m-diameter beam-waveguide antennas, the challenge lies in the following factors.

Low signal-to-noise ratio (SNR): The received deep-space signals have extremely low SNRs due to the small transmission power of a spacecraft and the large distances over which the signal is transmitted. Because the monopulse pointing-algorithm performance is proportional to the received SNR, the low SNR poses a challenge.

Large antenna structure: The structure of the 34-m-diameter antenna is susceptible to vibrations and to deformations due to thermal gradients, azimuth track unevenness, gravity loads, etc. A compensation technique is required to improve the antenna blind pointing. The structure also requires extended pointing performance of the antenna servo system that compensates for the antenna inertia and for flexibility in wind disturbances.

Distributed downlink system: The downlink system is distributed in physical distance relative to the frequency of the downlink signal. It introduces relative amplitude and phase distortion in signal routing. The signal-routing distances are up to a few feet at Ka-band frequencies and up to 15 km at the downconverted intermediate frequencies between 100 and 600 MHz.

Small pointing-error requirement: The required amplitude stability of a 0.1-dB gain requires a small pointing error due to the narrow width of the Ka-band beam. The required precision in mean radial error is approximately from 0.7 to 1.5 mdeg.

Specific perturbation factors that are accounted for in the analysis are

(1) Non-ideal finite null depth in the antenna–feed pattern

(2) Shift in bore sight in the antenna–feed pattern

(3) Additive (white) noise input

(4) Wind effect as seen by the encoder

(5) Encoder error due to discontinuities in the track (known)

(6) Servo residual error (known)

(7) Phase-calibration error between the main and error channels

Other sources of noise/perturbation assumed to be negligible in the analysis are

(1) Antenna deformation due to lateral and axial displacements due to gravitational force and wind impact on the structure

(2) Unaccounted pre- and post-comparator errors in amplitude and phase that degrade the effective antenna pattern

(3) Possible asymmetry in the beam-waveguide antenna pattern

(4) Quantization error

(5) Doppler dynamics in the target position

(6) Antenna and feed cross-polarization

(7) Tracking receiver drift (negligible in a digital receiver)

III. Monopulse Pointing System Design

The monopulse pointing system is composed of the following subsystems interleaved to function as a closed loop, as shown in Fig. 1:

(1) The antenna, monopulse feed, and low-noise amplifier (LNA) in the front end

(2) The Block V receiver (BVR)

(3) The antenna-pointing controller (APC)

The main and the error signals, $x_m(t)$ and $x_e(t)$, are at the output of the antenna and the monopulse feed. These signals have the same RF frequency and are related in amplitude and phase as functions of the antenna-pointing error in azimuth and elevation. In the receiver subsystem, the main and error signals are processed to estimate the antenna-pointing error from the known amplitude and phase relationship. In the antenna-pointing servo controller, the detected error is processed, and the antenna position is corrected by the processed amount. This feedback correction closes the monopulse tracking loop. Dictated by the physics of the antenna and feed structure and the servo control design for the DSN, the pointing-error detection, estimation, and correction occur at different parts of the system, referenced to the different coordinate systems; the coordinate systems are fully defined in Appendix A.

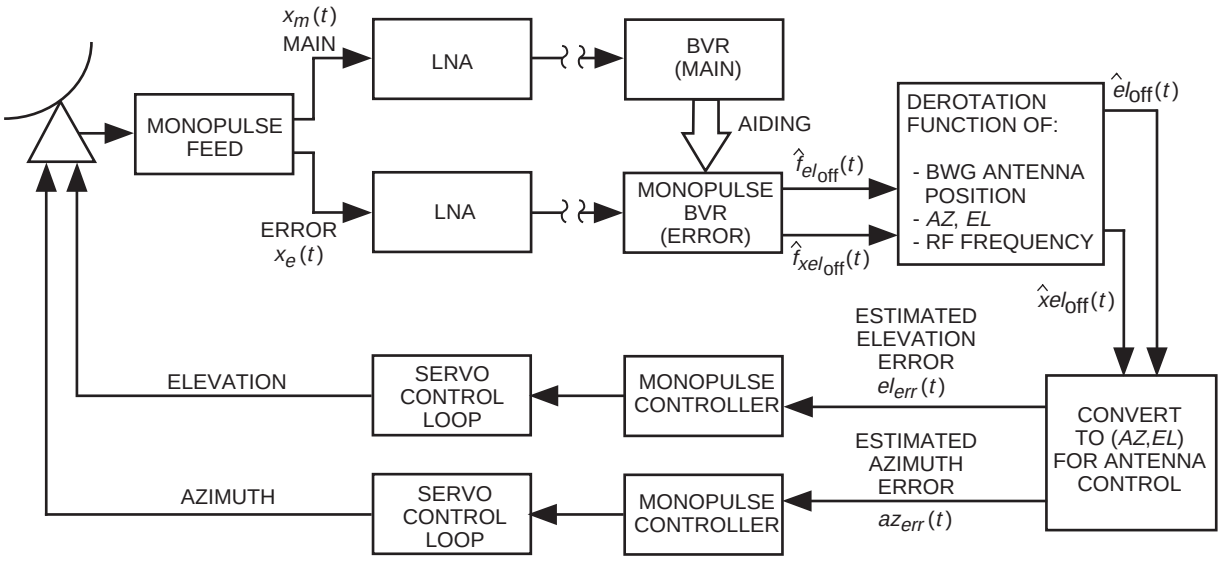

Fig. 1. The monopulse pointing design in the DSN 34-m beam-waveguide antennas.

A. Signal Flow Description in Fig. 1

The main and the error signals, $x_m(t)$ and $x_e(t)$, are the output of the antenna and monopulse feed:

$$x_m(t) = \sqrt{2P}\cos(\omega_{c,\mathrm{RF}}t + \theta_c + \Delta D(t)) + n_m(t) \tag{1}$$

$$x_e(t) = \sqrt{2P}\sqrt{g(\theta_F,\phi_F)}\cos(\omega_{c,\mathrm{RF}}t + \theta_c + \Delta D(t) + h(\theta_F,\phi_F)) + n_e(t) \tag{2}$$

where

$P =$ the received signal power

$[\omega_{c,\mathrm{RF}}, \theta_c] =$ the carrier frequency and phase of the received signal (at radio frequency)

$\Delta =$ the modulation index

$D(t) = d(t)\mathrm{Sgn}[\sin(\omega_{sc}t + \theta_{sc})]$

$=$ data $d(t)$ modulated on the subcarrier with frequency and phase $[\omega_{sc}, \theta_{sc}]$

$\mathrm{Sgn}[\cdot] =$ the sign of the argument

$\theta_F =$ the azimuth angle of the signal arrival at the feed (in a spherical coordinate system referenced to the feed [see Appendix A])

$\phi_F =$ the elevation angle of the signal arrival at the feed (in a spherical coordinate system referenced to the feed [see Appendix A])

$\sqrt{g(\theta_F,\phi_F)} \simeq \gamma\,\theta_F$

$=$ the ratio of the error signal amplitude and the main signal amplitude, as a function of (θ_F, ϕ_F) (see Appendix B)

$\gamma =$ the slope of $\sqrt{g(\theta_F,\phi_F)}$, the sensitivity factor

$h(\theta_F,\phi_F) \simeq \phi_F$

$=$ the difference between the main- and the error-channel phases, as a function of (θ_F, ϕ_F) (see Appendix B)

$n_m(t), n_e(t) =$ the additive white noise in the main and error channels

These signals are amplified independently in the LNAs:

$$x_{m,\mathrm{LNA}}(t) = \sqrt{2P}\cos(\omega_{c,\mathrm{RF}}t + \theta_c + \Delta D(t)) + n_{m,\mathrm{LNA}}(t) \tag{3}$$

$$x_{e,\mathrm{LNA}}(t) = \sqrt{2P}A_1\sqrt{g(\theta_F,\phi_F)}\cos(\omega_{c,\mathrm{RF}}t + \theta_c + \Delta D(t) + \Delta\phi_1 + h(\theta_F,\phi_F)) + n_{e,\mathrm{LNA}}(t) \tag{4}$$

where

$A_1 =$ the relative amplitude distortion between the main and error channels introduced by independent amplification

$\Delta\phi_1 =$ the relative phase distortion introduced by independent amplification

$n_{m,\mathrm{LNA}}(t), n_{e,\mathrm{LNA}}(t) =$ the additive white noise at the output of the LNAs, with noise spectral densities of $N_{o,m}$ and $N_{o,e}$, respectively

In the BVR, each signal is downconverted independently to the intermediate frequency (IF) and routed to the receiver channel processor (RCP) as $x_{m,\mathrm{BVR}}(t)$ and $x_{e,\mathrm{BVR}}(t)$ for the remainder of the receiver signal processing (this signal routing may be as far as 15 km from the beam-waveguide antenna to the signal-processing center):

$$x_{m,\mathrm{BVR}}(t) = \sqrt{2P}\cos(\omega_{\mathrm{IF}}t + \theta_{\mathrm{IF}} + \Delta D(t)) + n_{m,\mathrm{BVR}}(t) \tag{5}$$

$$x_{e,\mathrm{BVR}}(t) = \sqrt{2P}A\sqrt{g(\theta_F,\phi_F)}\cos(\omega_{\mathrm{IF}}t + \theta_{\mathrm{IF}} + \Delta D(t) + h(\theta_F,\phi_F) + \Delta\phi) + n_{e,\mathrm{BVR}}(t)$$

$$\simeq \sqrt{2P}A\gamma\theta_F\cos(\omega_{\mathrm{IF}}t + \theta_{\mathrm{IF}}\Delta D(t) + \phi_F + \Delta\phi) + n_{e,\mathrm{BVR}}(t) \tag{6}$$

where

$(\omega_{\mathrm{IF}}, \theta_{\mathrm{IF}}) =$ the carrier intermediate frequency and phase

$n_{m,\mathrm{BVR}}(\cdot), n_{e,\mathrm{BVR}}(\cdot) =$ the received additive noise at the BVR

$\Delta\phi =$ the relative phase distortion introduced by independent amplification, downconversion, and signal routing of $x_{m,\mathrm{BVR}}(t)$ and $x_{e,\mathrm{BVR}}(t)$, respectively

$A =$ the relative amplitude distortion between the main and error channels introduced by independent amplification, downconversion, and signal routing of $x_{m,\mathrm{BVR}}(t)$ and $x_{e,\mathrm{BVR}}(t)$, respectively; this distortion will be compensated for by calibration

Receiver processing of $x_{m,\mathrm{BVR}}(t)$ and $x_{e,\mathrm{BVR}}(t)$ is shown in Fig. 2 and described in Appendix C. The outputs of the receiver are estimates of the pointing error in the cross-elevation (xel_{off}) and elevation (el_{off}) coordinate system referenced to the feed. Represented as a two-dimensional vector,

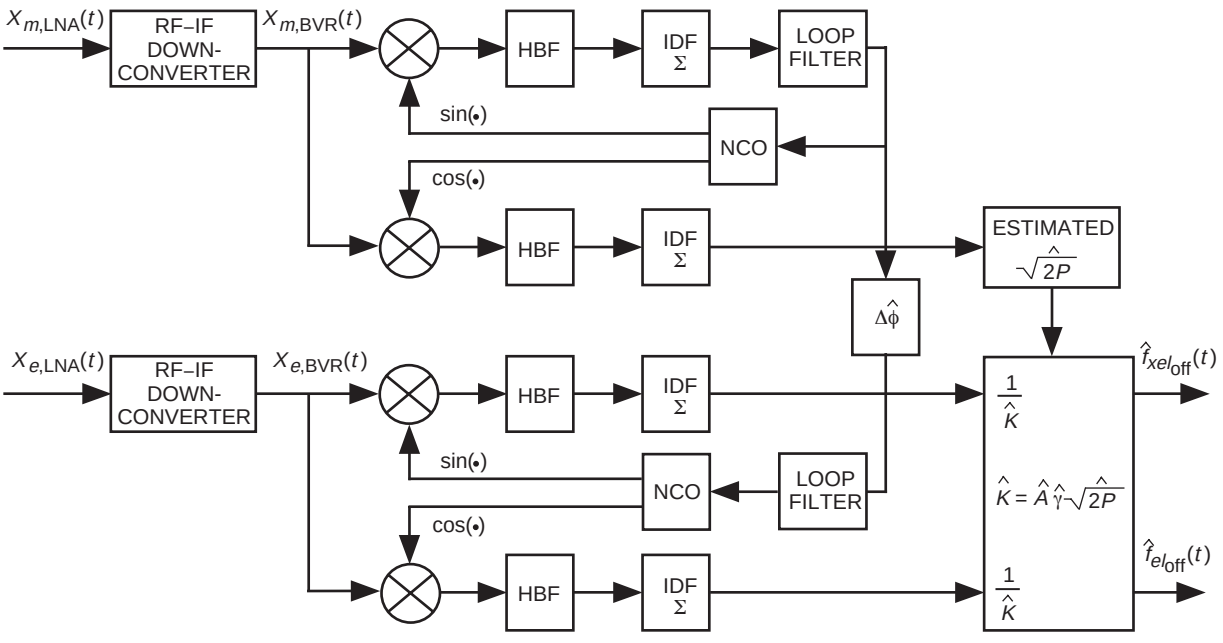

Fig. 2. The block diagram for receiver processing.

$$\begin{bmatrix} \hat{f}_{xel_{\rm off}}(t) \\ \hat{f}_{el_{\rm off}}(t) \end{bmatrix} = R_{\rm BVR} \begin{bmatrix} \cos(\Delta_{\phi,calib}) & -\sin(\Delta_{\phi,calib}) \\ \sin(\Delta_{\phi,calib}) & \cos(\Delta_{\phi,calib}) \end{bmatrix} \begin{bmatrix} f_{xel_{\rm off}} \\ f_{el_{\rm off}} \end{bmatrix} + \begin{bmatrix} n_{fxel}(t) \\ n_{fel}(t) \end{bmatrix} \tag{7}$$

where

$$\begin{aligned}
\hat{f}_{xel_{\rm off}}(t) &= \text{ the estimate of } f_{xel_{\rm off}} \\
\hat{f}_{el_{\rm off}}(t) &= \text{ the estimate of } f_{el_{\rm off}} \\
f_{xel_{\rm off}} &= -\theta_F \cos(\phi_F) \\
&= \text{ the true pointing error in the cross-elevation axis referenced to the feed (Appendix A)} \\
f_{el_{\rm off}} &= \theta_F \sin(\phi_F) \\
&= \text{ the true pointing error in the elevation axis referenced to the feed (Appendix A)} \\
R_{\rm BVR} &= \frac{A\gamma\sqrt{P}}{\hat{A}\hat{\gamma}\sqrt{\hat{P}}} \text{ (defined in Appendix C)} \\
n_{fxel}(t), n_{fel}(t) &= \text{ the additive noises defined in Appendix C}
\end{aligned}$$

In the antenna-pointing controller (APC), $[\hat{f}_{xel_{\rm off}}(t), \hat{f}_{el_{\rm off}}(t)]$ are derotated and converted azimuth and elevation angles in the antenna coordinates (see Appendix A for definitions and derivation):

$$\begin{bmatrix} \hat{a}z_{err}(t) \\ \hat{e}l_{err}(t) \end{bmatrix} = \frac{1}{\hat{\Lambda}} \times \begin{bmatrix} \dfrac{1}{\cos[el]} & 0 \\ 0 & 1 \end{bmatrix} \begin{bmatrix} \cos\left(\hat{\phi}_{derot}\right) & -\sin\left(\hat{\phi}_{derot}\right) \\ \sin\left(\hat{\phi}_{derot}\right) & \cos\left(\hat{\phi}_{derot}\right) \end{bmatrix} \begin{bmatrix} \hat{f}_{xel_{\rm off}} \\ \hat{f}_{el_{\rm off}} \end{bmatrix} \tag{8}$$

where

$$\begin{aligned}
\hat{\Lambda} &= \text{ the best estimate of (BDF} \times G_{aberr} \times R_{\rm BVR}) \\
\hat{\phi}_{derot} &= \hat{\phi}_{\rm rotate} + \hat{\phi}_{aberr} = \text{ the best estimated derotation angle} \\
\hat{\phi}_{\rm rotate} &= \text{ the estimate of } \phi_{\rm rotate} \\
\hat{\phi}_{aberr} &= \text{ the estimate of } \phi_{aberr}
\end{aligned}$$

Algebraic follow-through shows that

$$\begin{bmatrix} \hat{a}z_{err}(t) \\ \hat{e}l_{err}(t) \end{bmatrix} = A_\Lambda \begin{bmatrix} \cos(\phi_\Delta) & -\sin(\phi_\Delta) \\ \sin(\phi_\Delta) & \cos(\phi_\Delta) \end{bmatrix} \begin{bmatrix} az_{err}(t) \\ el_{err}(t) \end{bmatrix} + \begin{bmatrix} n_{az}(t) \\ n_{el}(t) \end{bmatrix} \tag{9}$$

where

$$A_\Lambda = \frac{\Lambda}{\hat{\Lambda}} \tag{10}$$

$$\phi_\Delta = \Delta_{\phi,calib} + (\phi_{\rm rotate} - \hat{\phi}_{\rm rotate}) + (\phi_{aberr} - \hat{\phi}_{aberr})$$

In summary, the estimated vector, $\overrightarrow{\hat{Z}} \equiv \begin{bmatrix} \hat{a}z_{err}(t) \\ \hat{e}l_{err}(t) \end{bmatrix}$, is equal to the true vector, $\overrightarrow{Z} \equiv \begin{bmatrix} az_{err}(t) \\ el_{err}(t) \end{bmatrix}$, scaled by A_Λ and rotated in two-dimensional space by angle ϕ_Δ, with an added noise vector, $\begin{bmatrix} n_{az}(t) \\ n_{el}(t) \end{bmatrix}$ (illustrated in Fig. 3).

The estimated pointing-error values, $\begin{bmatrix} \hat{a}z_{err}(t) \\ \hat{e}l_{err}(t) \end{bmatrix}$, are fed into the servo controller, where they are processed. To combat the effects of wind, an aggressive controller design, the linear-quadratic-Gaussian (LQG) controller, will be adopted [2]. The processed values are used to correct the position of the antenna, thus closing the monopulse loop.

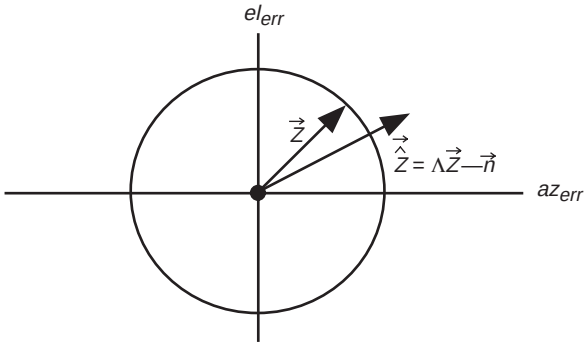

Fig. 3. The estimated pointing-error vector versus the true pointing-error vector.

B. Behavioral Description of Closed-Loop Tracking Dynamics in the Two-Dimensional Closed Loop

Modeling the monopulse system as a two-dimensional feedback system in azimuth and elevation, let $\overrightarrow{Z} \equiv \begin{bmatrix} az_{err}(t) \\ el_{err}(t) \end{bmatrix}$ be the pointing error at a given time. In the ideal case, applying the perfect correction vector, $\overrightarrow{C} \equiv -\overrightarrow{Z}$, to the loop will reduce the error to zero [Fig. 4(a)]. For the case discussed here, the two-dimensional acquisition process is shown in Fig. 4(b), where "X" marks the target and the origin represents the initial antenna point. The dashed line shows the instantaneous position of antenna pointing en route to the target. In this case, the dashed line follows a direct path to acquiring lock onto the target.

However, with the estimated pointing error shown in Fig. 3, the correction is not perfect:

$$\overrightarrow{C} = -\begin{bmatrix} \hat{a}z_{err}(\cdot) \\ \hat{e}l_{err}(\cdot) \end{bmatrix} = -A_\Lambda \begin{bmatrix} \cos(\phi_\Delta) & -\sin(\phi_\Delta) \\ \sin(\phi_\Delta) & \cos(\phi_\Delta) \end{bmatrix} \overrightarrow{Z} - \overrightarrow{n} \tag{11}$$

from Eq. (9), where

$$\overrightarrow{n} = \begin{bmatrix} n_{az}(t) \\ n_{el}(t) \end{bmatrix} \tag{12}$$

For the case when $\overrightarrow{C}$ is reasonably close to $\overrightarrow{Z}$, $\overrightarrow{C}$ reduces but does not perfectly compensate for $\overrightarrow{Z}$ [illustrated in Fig. 5(a)]. With each feedback indexed i, the two-dimensional pointing error will decrease in magnitude as long as the following holds:

$$|\overrightarrow{Z}_{i+1}| = |-A_\Lambda \overrightarrow{Z}_i + \overrightarrow{n}_i - \overrightarrow{Z}_i| < |\overrightarrow{Z}_i|$$

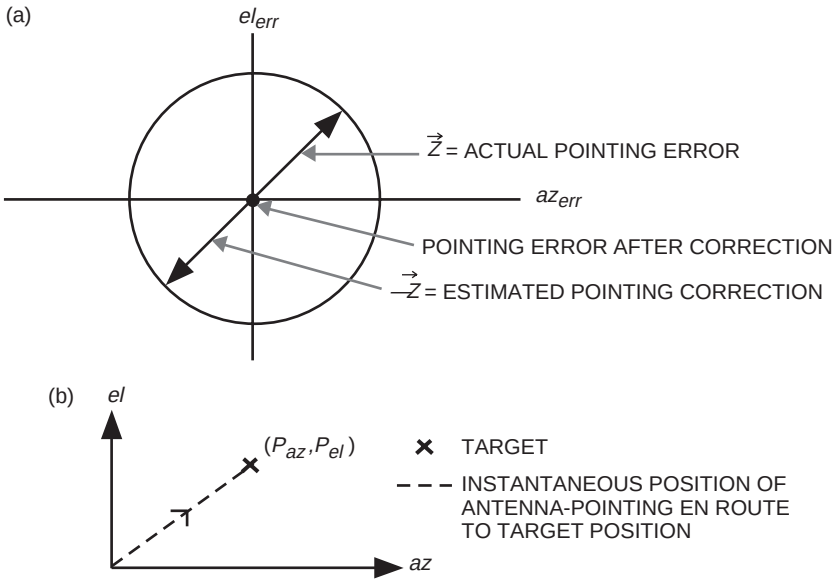

Fig. 4. The ideal case for pointing-error correction: (a) perfect pointing-error correction in two-dimensional space and (b) ideal transient response in target acquisition.

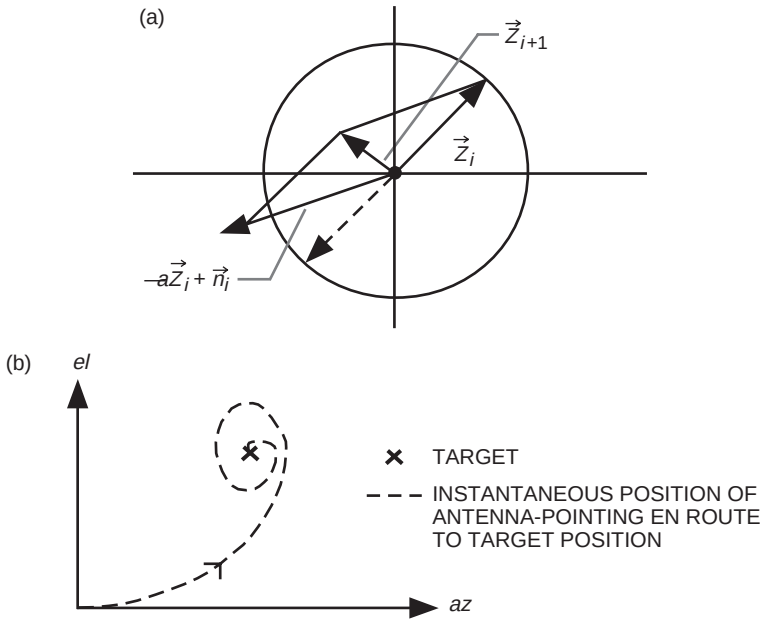

Fig. 5. The non-ideal case for pointing-error correction: (a) imperfect pointing-error correction in two-dimensional space and (b) non-ideal transient response in target acquisition.

i.e., as long as

$$|\overrightarrow{n}_i - (A_\Lambda - 1)\overrightarrow{Z}_i| < |\overrightarrow{Z}_i| \tag{13}$$

For this case, the pointing error is corrected in a meandering pattern that converges near the target, as shown in Fig. 5(b). At some point along the decreasing $|\overrightarrow{Z}_i|$ process, the noise amplitude exceeds the

needed correction, and the above condition no longer is valid. At this point, the error $\overrightarrow{Z}$ will wander within a circle of radius $\theta_{e,max}$, as shown in Fig. 6. The radius $\theta_{e,max}$ depends on the noise characteristics, $\overrightarrow{n}_i$.

In summary, given an initial pointing error, $\overrightarrow{Z}_0$, the monopulse loop recursively reduces the error through feedback until the noise limit is reached. At that point, the pointing error wanders within the noise limit radius, $\theta_{e,max}$, which represents the performance limit of the loop.

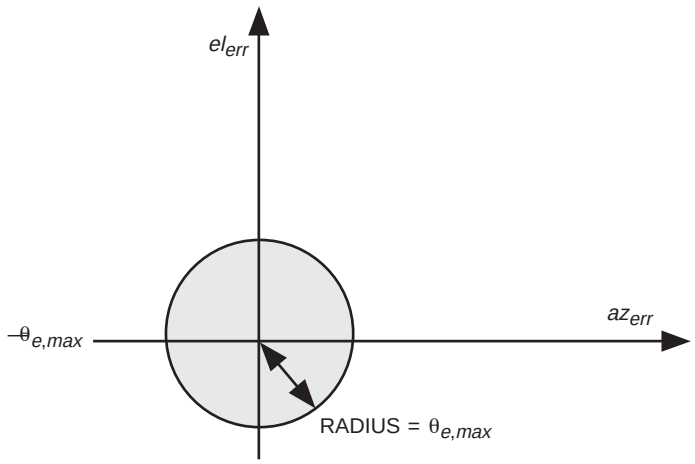

Fig. 6. Loci of the pointing error during in-lock status.

IV. Analysis of the Monopulse Tracking Loop

A block diagram of the monopulse system is shown in Fig. 7. An analytically equivalent model of the monopulse loop is shown in Fig. 8, where the dashed circles show the system perturbations and their injection points into the system. Assuming independence between the azimuth and elevation axes of the antenna, the model can be simplified to Fig. 9. (In reality, there exists a very weak correlation between the two axes.) Each feed-back loop for el_{off} and xel_{off} is analogous to a phase-locked loop (PLL) [3]:

(1) The antenna–feed–receiver combination is analogous to the combination of the phase-error detector and the follow-on integrator for improved SNR.

(2) The servo controller in the APC is analogous to the loop filter.

(3) The combination of the servo controller and antenna correction is analogous to the numerically controlled oscillator (NCO) and feedback in a PLL.

Each loop is analyzed as a PLL, as shown in Fig. 10. The output, θ_{out}, is equivalent to the estimate of the input phase, θ_{in}, and the quality of the phase-locked-loop tracking is determined by the tracking-error variance, $\text{var}[\theta_{\text{in}} - \theta_{\text{out}}]$. Note that $\text{var}[\theta_{\text{in}} - \theta_{\text{out}}]$ is equal to $\text{var}[xel_{\text{off}} - \hat{x}el_{\text{off}}]$ in the cross-elevation loop and equal to $\text{var}[el_{\text{off}} - \hat{e}l_{\text{off}}]$ in the elevation loop.

The $\text{var}[\theta_{\text{in}} - \theta_{\text{out}}]$ depends on the noise components injected to the loop and on the loop characteristics. The individual contribution of each perturbation to $\text{var}[\theta_{\text{in}} - \theta_{\text{out}}]$ is evaluated as being filtered through the transfer function between the point of injection and the output, θ_{out}, of the loop. For this purpose, the following transfer functions and their bandwidths are defined:

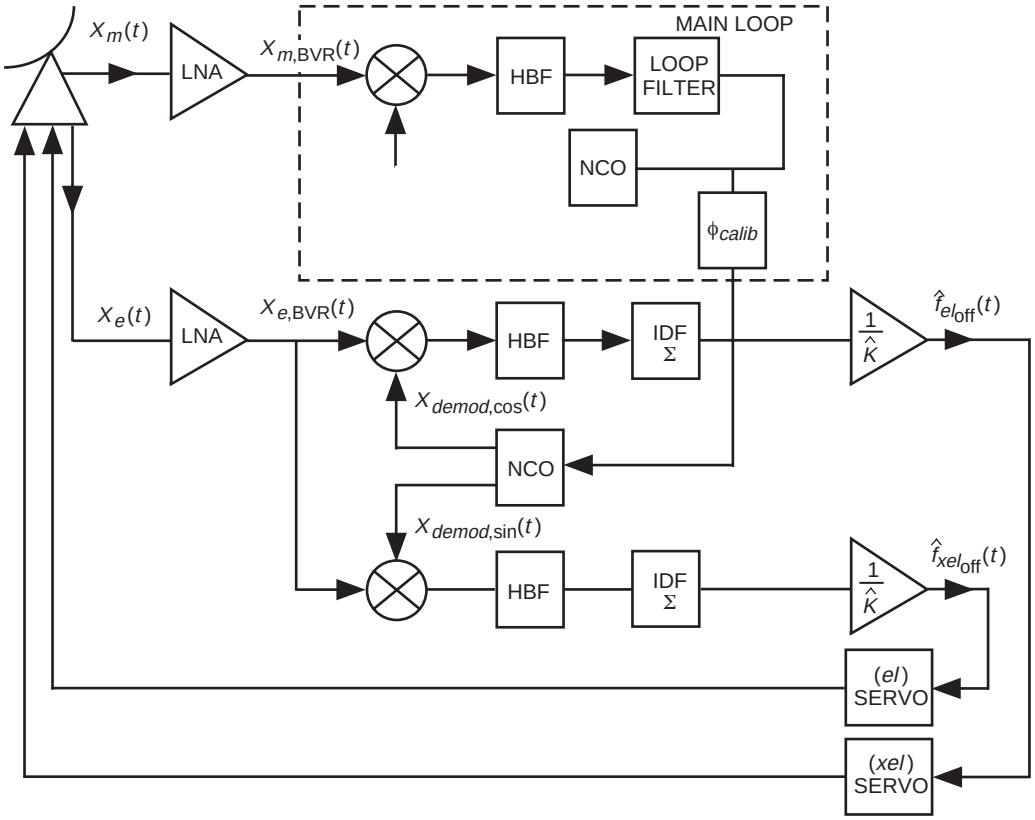

Fig. 7. The monopulse loop block diagram.

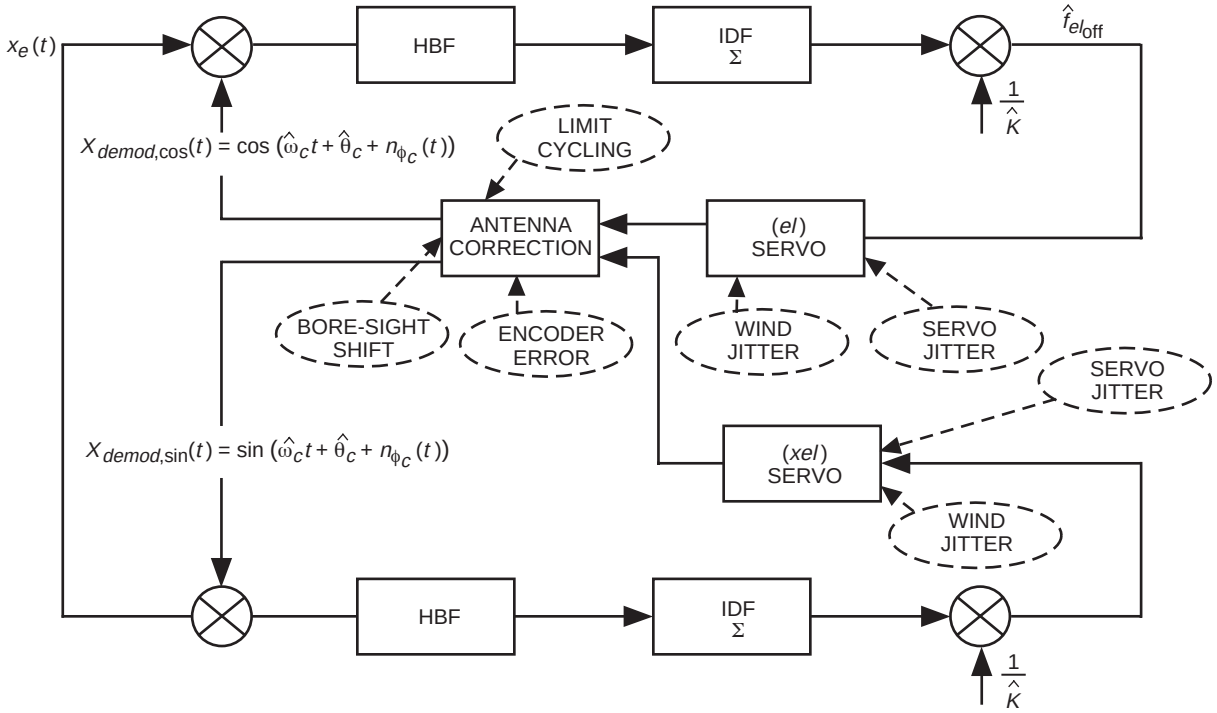

Fig. 8. An equivalent monopulse loop with system perturbations.

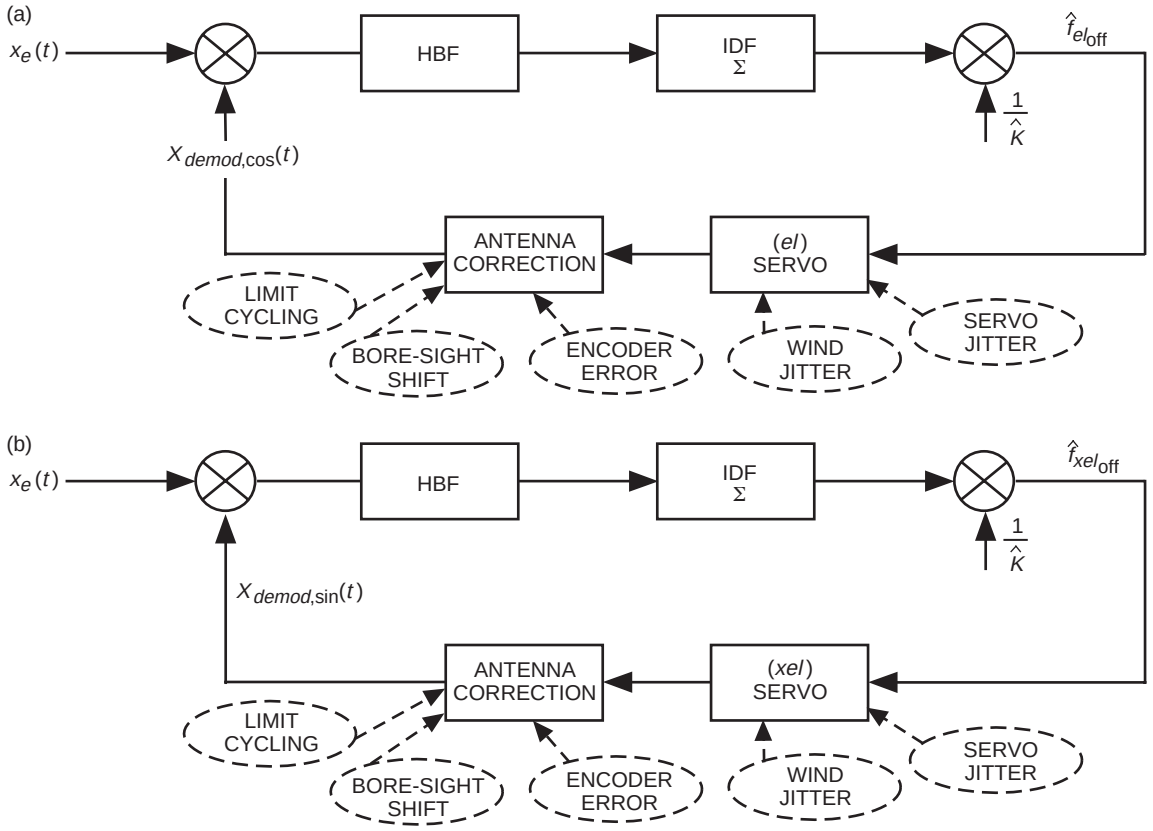

Fig. 9. Independent monopulse loop models: (a) elevation tracking loop and (b) cross-elevation tracking loop.

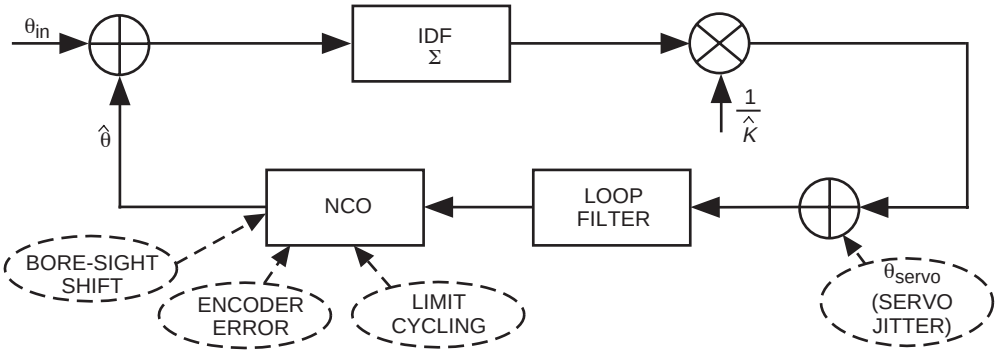

Fig. 10. The equivalent PLL.

(1) The transfer function between the input and the output is

$$H_m[s] \equiv \frac{\Theta_{\text{out}}[s]}{\Theta_{\text{in}}[s]} \tag{14}$$

with noise equivalent bandwidth $B_{L,m}$.

(2) The disturbance transfer function between the servo noise injection point and the output is defined as

$$H_r[s] \equiv \frac{\Theta_{\text{out}}[s]}{\Theta_{\text{in,servo}}[s]} \tag{15}$$

with noise equivalent bandwidth $B_{L,r}$.

For DSN BWG antennas, the structure of the azimuth and elevation loops are similar, and the closed-loop transfer functions are approximately the same. They can be estimated as [5]

$$H_m[s] \simeq \frac{\omega_o^2}{s^2 + 2\xi\omega_o s + \omega_o^2} \tag{16}$$

$$H_r[s] \simeq \frac{2\xi\omega_o s}{s^2 + 2\xi\omega_o s + \omega_o^2} \tag{17}$$

where

$$\omega_o = \sqrt{\frac{k}{T}} \tag{18}$$

$$\xi = \frac{1}{2\sqrt{kT}}$$

where k and T are second-order loop parameters. The parameters of the LQG filter are as shown in the following table:

T, s	k, s^{-1}	ω_o, rad	f_o, Hz	ξ	$B_{L,m}$, Hz	$B_{L,r}$, Hz
0.159	1	2.51	0.4	1.25	0.4	0.4

V. Performance of the Monopulse Loop

In the following two subsections, performance of the monopulse loop is assessed in terms of (1) statistical expectation of error jitter in estimates of the cross-elevation and elevation pointing and (2) transient response in acquiring the target.

A. Pointing-Error Jitter

The goal of the monopulse design is to minimize the amount of jitter in the pointing error. For performance assessment, the mean radial error (MRE) is used as an error metric. It is defined as

$$\text{MRE} \equiv E\left[\sqrt{(xel_{\text{off}} - \hat{x}el_{\text{off}})^2 + (el_{\text{off}} - \hat{e}l_{\text{off}})^2}\right] \tag{19}$$

where $E[\cdot]$ denotes statistical expectation.

For DSN BWG antennas, the MRE is coarsely approximated as[4]

$$\text{MRE} \simeq \sqrt{\frac{\pi}{2}}\sqrt{\frac{1}{2}\left(\sigma_{xel}^2 + \sigma_{el}^2\right)} \tag{20}$$

The standard deviations of errors, σ_{xel}^2 and σ_{el}^2, in the xel_{off} and el_{off} estimates, respectively, are approximated by the root of the sum of the squares (RSS) of independent perturbations in the equivalent loop shown in Fig. 10, i.e.,

$$\sigma_{xel} = \sqrt{\frac{\sigma_{\text{limit cycle}}^2}{2} + \sigma_{\text{sys noise}}^2 + \sigma_{\text{servo}}^2 + \sigma_{enc}^2 + \sigma_{\text{wind},AZ}^2} \tag{21}$$

$$\sigma_{el} = \sqrt{\frac{\sigma_{\text{limit cycle}}^2}{2} + \sigma_{\text{sys noise}}^2 + \sigma_{\text{servo}}^2 + \sigma_{\text{wind},EL}^2} \tag{22}$$

where

$\sigma_{\text{limit cycle}}^2 =$ the pointing error due to limit cycling caused by finite null depth in the antenna–feed pattern

$\sigma_{\text{sys noise}}^2 =$ the pointing error due to the additive white noise at the input of the monopulse system

$\sigma_{\text{servo}}^2 =$ the pointing error due to servo noise

$\sigma_{enc}^2 =$ the pointing error due to encoder imperfections

$\sigma_{\text{wind},AZ}^2 =$ the pointing error in the azimuth axis due to wind disturbances

$\sigma_{\text{wind},EL}^2 =$ the pointing error in the elevation axis due to wind disturbances

Each component in Eqs. (21) and (22) is analyzed individually in the following subsections.

1. Limit Cycling ($\sigma_{\text{limit cycle}}^2$). Limit cycling results from a non-ideal null depth that is due to (a) decrease in slope near $\theta = 0$ and (2) a non-negligible feedback value near $\theta = 0$. See Appendix B for the full derivation. Jitter on the monopulse loop due to limit cycling is

$$\sigma_{\text{limit}}^2 \simeq \frac{\theta_{\text{limit}}^2}{2} \tag{23}$$

For DSN BWG antennas,

$$\theta_{\text{limit}}(N') = 0.0014 \times 10^{-([N'(\text{dB})]/20)} \tag{24}$$

[4] In the coarse approximation, it is assumed that $(xel_{\text{off}} - \hat{x}el_{\text{off}})$ and $(el_{\text{off}} - \hat{e}l_{\text{off}})$ are Gaussian-distributed random variables, and the approximation is an extrapolation from the case when variables X and Y are equally distributed and Gaussian, i.e., $\sigma_{\text{single axis}}^2 \equiv \text{var}[X] = \text{var}[Y]$, where the term $\sqrt{X^2 + Y^2}$ can be approximated as a Raleigh distribution sample with a mean of $\sqrt{\pi/2}\sigma_{\text{single axis}}$ and a variance of $\sigma_{\text{single axis}}^2(2 - [\pi/2])$.

2. System Noise ($\sigma^2_{\text{sys noise}}$). Phase jitter contribution due to additive noise at the input of the system, analyzed in Appendix D, is

$$\sigma^2_{\text{sys noise}} = \frac{1}{\hat{\gamma}^2} R_{\text{BVR}} \left(\frac{A}{\hat{A}} \right)^2 \times \frac{N_{o,e} B_{L,m}}{P_{c,m}} \tag{25}$$

3. Servo Jitter (σ^2_{servo}). Servo jitter is a noise in the servo loop, observed even if no apparent disturbances, such as wind gusts, are detected. Its contribution to the monopulse pointing jitter is given as

$$\sigma^2_{\text{servo}} \simeq N_{o,\text{servo}} B_{L,r} \tag{26}$$

where $N_{o,\text{servo}}$ = the spectral density of the servo noise. It is available through field measurements.

4. Wind Disturbances (σ^2_{wind}). The wind disturbance model is taken from the field measured data [4], and $\sigma^2_{\text{wind},AZ}$ and $\sigma^2_{\text{wind},EL}$ are derived from running the wind model through the monopulse loop model.

5. Encoder Imperfections (σ^2_{enc}). In Eq. (21), σ^2_{enc} is jitter contribution due to azimuth encoder imperfections. Originally, components of imperfection consisted of the radial run-out error, manufacturing tolerances, and rapid changes due to the gaps between the encoder rack segments. Recently, the gaps were eliminated by installing a solid one-piece encoder rack, consequently reducing σ^2_{enc} significantly.[5]

B. Non-Ideal Transient Response

Non-ideal transient response in acquiring the target pointing described in Section III.B can be caused by the following factors in the system.

1. Low-Noise Amplification. The independent amplification introduces imbalance in amplitude, A_1, and phase, $\Delta\phi_1$, relations between the main and error channels [in Eqs. (3) and (4)].

2. Calibration Between $x_m(\cdot)$ and $x_e(\cdot)$. Independent low-noise amplification, RF-to-IF down-conversion, and signal routing introduce amplitude and phase imbalance, $(A, \Delta\phi)$, between the main and the error channels [in Eqs. (5) and (6)]. These components are to be calibrated as closely as possible in the implementation. Residual phase imbalance leads to a longer acquisition time as the loop tracks through an indirect route to the lock point, as described in Section III.B [see Fig. 5(b)].

VI. Predicted and Simulated Performance Data

In this section, the predicted and simulated performances for the DSN BWG antennas are presented.

The predicted values are evaluated from Eqs. (20), (21), and (22).

The simulation results presented are obtained from the two-dimension simulations made using the equivalent model shown in Fig. 11. The azimuth and elevation axes were simulated jointly, portraying the weak correlation that exists due to the feed patterns being functions of both axes. Other physical/structural correlations that may exist were not included. The simulation included predicted antenna

[5] H. Ahlstrom, "DSS 26 Az Encoder Gear Measurements," JPL Interoffice Memorandum 3337-98-004 (internal document), Jet Propulsion Laboratory, Pasadena, California, February 9, 1997.

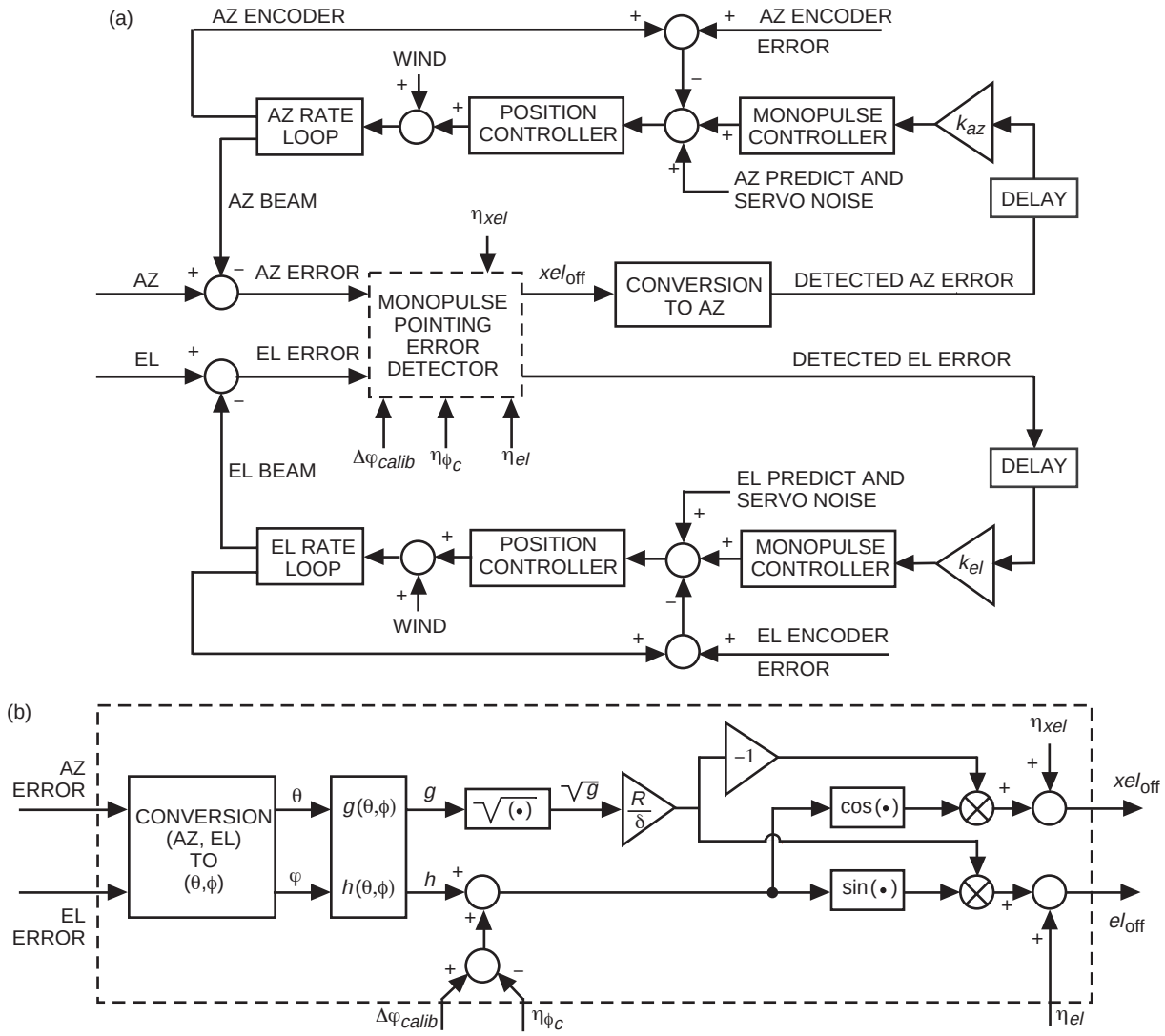

Fig. 11. Block diagrams of (a) the nonlinear monopulse control model and (b) the monopulse pointing-error detector.

patterns, receiver signal-processing equations, and the actual servo filter parameters. Measured values of wind and servo jitter were injected into the simulation. For the encoder non-linearity, σ^2_{enc} in Eq. (21) was derived from measured values of the segmented encoder gear rack run through a model of the monopulse loop. Since the segmented problem has been reduced significantly (see Section V.A.5), the predicted and simulated results in this article are pessimistic.

In the following subsections, the predicted and simulated mean radial errors are shown for

$$\text{null depth} = 35 \text{ dB and } 15 \text{ dB}$$

$$B_{L,m} = B_{L,r} = 0.4 \text{ Hz}$$

$$\text{phase calibration error in entire loop} = 25 \text{ deg}$$

$$\text{bore-sight shift} = 0.5 \text{ mdeg}$$

$$\sigma_{enc} = \text{ 0.1 mdeg (highly pessimistic based upon the segmented encoder design)}$$

$$\sigma_{\text{servo}} = \text{ 0.1 mdeg (based upon measured statistics)}$$

$$\text{wind input} = \text{ injected field-measured (24 km/h) wind model into the simulation}$$

$$\frac{P_{c,m}}{N_{o,e}} \text{ (dB-Hz)} = \text{ variable}$$

A. Simulated Plots of Monopulse Loop Behavior

In Fig. 12, simulation results confirming the loop behavior discussed in Section III.B [Fig. 5(b)] are shown for various SNRs. In the simulation, the antenna acquires the target at (az = 5 mdeg, el = 5 mdeg), starting from the origin in the (az, el) plane. Figures 12 (a) through (d) show the transient acquisition response path and lock points of the system for a decreasing value of SNR, $P_{c,m}/N_{o,e} = \{40, 27, 23, 17\}$ dB-Hz. As expected, the radius of the noise limit increases with a decrease in SNR. The acquisition path does not follow a straight line to the target due to the 25-deg phase-calibration error. After acquisition, pointing error wanders randomly within a circle about the target. The size of this circle indicates the extent of the mean radial error, which clearly increases with decrease in the SNR.

In Figs. 13(a) through (d), simulated measures of radial error as a function of time are shown for $P_{c,m}/N_{o,e} = \{40, 27, 23, 17)$ dB-Hz. As expected, the mean of the radial error increased with decrease in the SNR.

B. Predicted Versus Simulated Mean Radial Errors

Predicted versus simulated mean radial errors are summarized in Figs. 14 and 15 as a function of SNR for a null depth of 35 dB and 15 dB, respectively. The predicted and simulated MRE errors agreed well for a null depth of 35 dB. For 15 dB, the prediction was slightly pessimistic as compared with the simulated output.

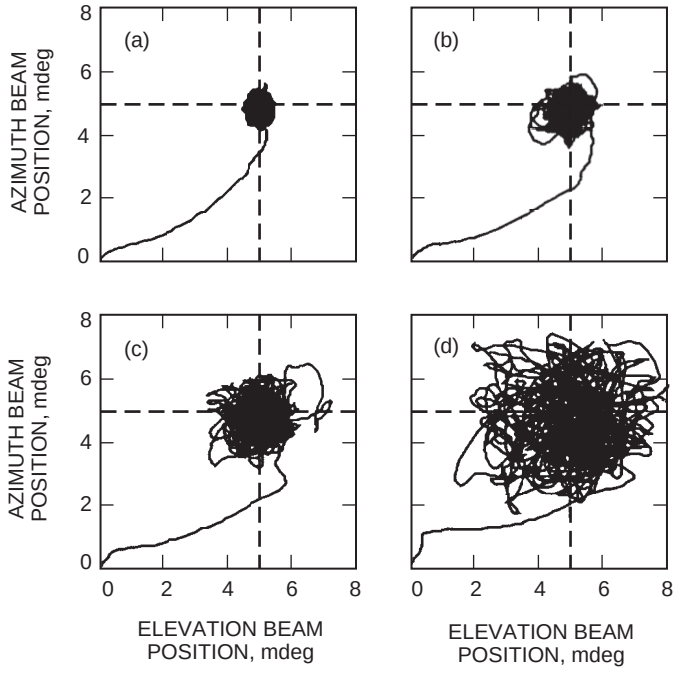

Fig. 12. Pointing as a function of time during acquisition and lock for a $P_{c,m}$ / $N_{o,e}$ of (a) 40 dB-Hz, (b) 27 dB-Hz, (c) 23 dB-Hz, and (d) 17 dB-Hz.

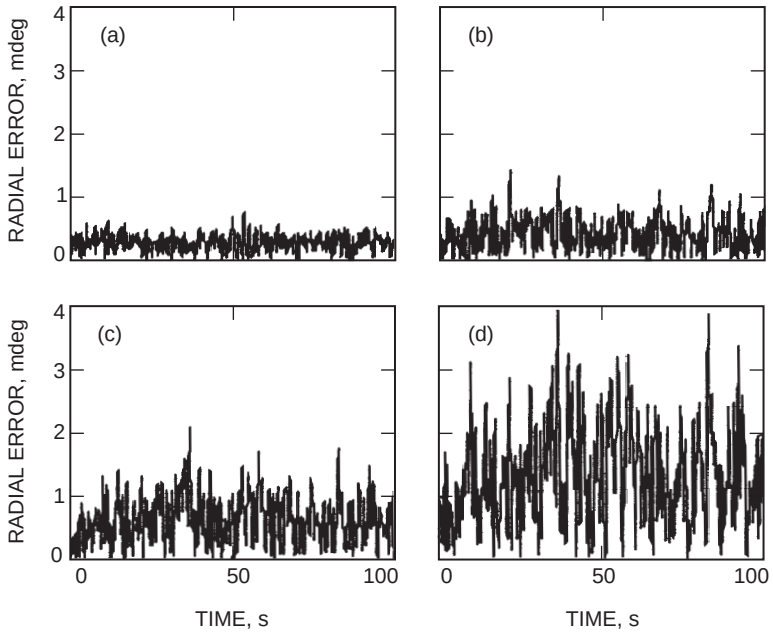

Fig. 13. Pointing radial error as a function of time for a $P_{c,m}/N_{o,e}$ of (a) 40 dB-Hz, (b) 27 dB-Hz, (c) 23 dB-Hz, and (d) 17 dB-Hz.

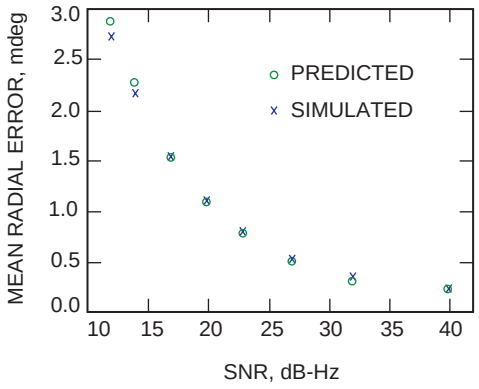

Fig. 14. The predicted compared to the simulated mean radial error for a 35-dB null depth as a function of SNR = $P_{c,m}/N_{o,e}$.

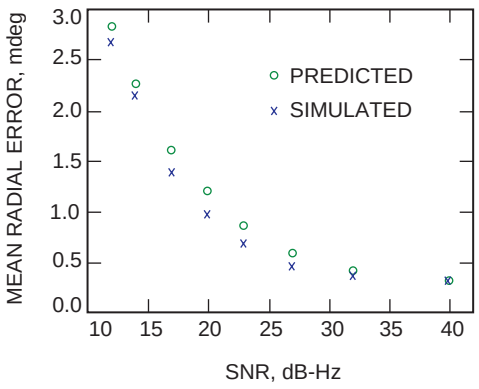

Fig. 15. The predicted compared to the simulated mean radial error for a 15-dB null depth as a function of SNR = $P_{c,m}/N_{o,e}$.

C. Summary of Performance Results

The results given in this section confirm the analytically described loop behavior discussed in Section III.B. These results also show that the prediction model is reasonable, and they confirm that the Cassini radio science requirement of an MRE less than or equal to 1.5 mdeg can be met down to approximately 17 dB-Hz in$P_{c,m}/N_{o,e}$.

The simulation model also is useful for testing sensitivity of the loop to various imperfections and perturbations that are encountered during implementation.

VII. Conclusion

In this article, the monopulse pointing system for the DSN beam-waveguide antennas was analyzed. Acquisition and tracking behavior were described analytically, and the pointing performance was analyzed in terms of the variance of the pointing error during spacecraft tracking and transient response in the acquisition process. Simulation results obtained from two-axes simulation in azimuth and elevation showed agreement with the predicted results. The analysis, simulation, and design presented in this article serve as a good performance prediction as well as a useful aid to identifying implementation errors that can contribute to degradation of the performance. The simulation model can be further utilized to test for sensitivity of the loop to any obvious imperfections encountered in implementation. Results show that, when properly implemented, this technique will meet the Cassini radio science requirement of an MRE less than or equal to 1.5 mdeg down to reasonable SNRs.

Acknowledgments

The authors would like to thank L. Alvarez for servo-noise analysis; A. Prata for antenna–feed pattern degradation-model analysis; P. Kinman for analytical review of the article; S. Petty for analysis of the low-noise amplifier performance; M. Berg for providing information on the antenna-pointing controller implementation; W. Hodgin for technical review; and E. W. Stone, M. Gatti, and M. Thorburn for technical management.

References

[1] Y. H. Choung, K. R. Goudey, and L. G. Bryans, "Theory and Design of a Ku-Band TE_{21}-Mode Coupler," *IEEE Transactions on Microwave Theory and Techniques*, vol. 30, no. 11, November 1982.

[2] W. Gawronski, C. Racho, and J. Mellstrom, "Application of the LQG and Feedforward Controllers for the DSN Antennas," *IEEE Transactions on Control Systems Technology*, vol. 3, 1995.

[3] F. M. Gardner, *Phaselock Techniques*, New York: John Wiley & Sons, Inc., 1979.

[4] W. Gawronski, "Wind Gust Models Derived From Field Data," *The Telecommunications and Data Acquisition Progress Report 42-123, July–September 1995*, Jet Propulsion Laboratory, Pasadena, California, pp. 30–36, November 15, 1995. http://tmo.jpl.nasa.gov/tmo/progress_report/42-123/123G.pdf

[5] W. Gawronski and M. A. Gudim, "Design and Performance of the Monopulse Control System," *The Telecommunications and Mission Operations Progress Report 42-137, January–March 1999*, Jet Propulsion Laboratory, Pasadena, California, pp. 1–15, May 15, 1999. http://tmo.jpl.nasa.gov/tmo/progress_report/42-137/137A.pdf

Appendix A
Coordinate Systems in the Monopulse Loop

Dictated by the physics of the antenna and feed structure, signal-processing, and servo control design, the pointing-error detection, estimation, and correction occur at different parts of the system, referenced to the different coordinate systems, as illustrated in Fig. A-1. The signal collected by the antenna dish and routed to the feed contains information on pointing-error magnitude and direction, (θ, ϕ), in a spherical coordinate system referenced to the antenna elevation (tipping) structure. This pointing error is sensed at the feed, (θ_f, ϕ_f), in a spherical coordinate system referenced to the feed, which is in a fixed location in the antenna pedestal. To recover pointing errors useful to the antenna servo, the receiver transforms θ_f and ϕ_f into Cartesian coordinates, $(f_{xel_{\text{off}}}, f_{el_{\text{off}}})$. The $f_{xel_{\text{off}}}$ and $f_{el_{\text{off}}}$ are derotated to tipping-structure cross-elevation and elevation, $xel_{\text{off}}, el_{\text{off}}$, within the APC, which then transforms xel_{off} and el_{off} to antenna coordinates azimuth and elevation. The different coordinate systems are illustrated in Fig. A-2 and defined below.

The relationship between (θ, ϕ) and (θ_F, ϕ_F) is

$$\left.\begin{aligned} \theta_F &= \theta \times \frac{1}{\text{BDF} \times G_{aberr}} \\ \phi_F &= \phi - \phi_{\text{rotate}} - \phi_{aberr} \end{aligned}\right\} \tag{A-1}$$

where

$\text{BDF} =$ the antenna amplification factor

$\phi_{\text{rotate}} = AZ - EL - \tau$

$AZ =$ the instantaneous azimuth position of the antenna

$EL =$ the instantaneous elevation position of the antenna

$\tau =$ the parameter dependent upon the physical location of the feed within the antenna pedestal

$G_{aberr} =$ the loss factor due to aberration effects

$\phi_{aberr} =$ the phase distortion due to aberration effects

A vector in the feed coordinates is equal to a vector in antenna coordinates scaled by factor $1/(\text{BDF} \times G_{aberr})$ and rotated in phase by $-(\phi_{\text{rotate}} + \phi_{aberr})$.

The relationship between (θ_F, ϕ_F) and $(f_{xel_{\text{off}}}, f_{el_{\text{off}}})$ is

$$\left.\begin{aligned} f_{xel_{\text{off}}} &= -\theta_F \sin(\phi_F) \\ f_{el_{\text{off}}} &= \theta_F \cos(\phi_F) \end{aligned}\right\} \tag{A-2}$$

For the relationship between $(f_{xel_{\text{off}}}, f_{el_{\text{off}}})$ and $(xel_{\text{off}}, el_{\text{off}})$, the vectors $(f_{xel_{\text{off}}}, f_{el_{\text{off}}})$ and $(xel_{\text{off}}, el_{\text{off}})$ are related by the amplification factor $(\text{BDF} \times G_{aberr})$ and the phase rotation by $(AZ - EL - \tau)$:

$$\begin{bmatrix} xel_{\text{off}} \\ el_{\text{off}} \end{bmatrix} = \text{BDF} \times G_{aberr} \times \begin{bmatrix} \cos(\phi_{\text{rotate}} + \phi_{aberr}) & -\sin(\phi_{\text{rotate}} + \phi_{aberr}) \\ \sin(\phi_{\text{rotate}} + \phi_{aberr}) & \cos(\phi_{\text{rotate}} + \phi_{aberr}) \end{bmatrix} \begin{bmatrix} f_{xel_{\text{off}}} \\ f_{el_{\text{off}}} \end{bmatrix} \tag{A-3}$$

For the relationship between $(xel_{\text{off}}, el_{\text{off}})$ and (az_{err}, el_{err}), the cross-elevation and elevation, (xel, el), are two-dimensional coordinates relative to the tipping structure. The transformation to antenna azimuth and elevation is

$$\left.\begin{aligned} az_{err} &= \frac{xel_{\text{off}}}{\cos(el - \text{angle})} \\ el_{err} &= el_{\text{off}} \end{aligned}\right\} \tag{A-4}$$

where $el -$ angle is equal to the elevation angle of the antenna. Hence,

$$\begin{bmatrix} az_{err} \\ el_{err} \end{bmatrix} = \text{BDF} \times G_{aberr} \times \begin{bmatrix} \dfrac{1}{\cos(el - \text{angle})} & 0 \\ 0 & 1 \end{bmatrix} \times \begin{bmatrix} \cos(\phi_{\text{rotate}} + \phi_{aberr}) & -\sin(\phi_{\text{rotate}} + \phi_{aberr}) \\ \sin(\phi_{\text{rotate}} + \phi_{aberr}) & \cos(\phi_{\text{rotate}} + \phi_{aberr}) \end{bmatrix} \begin{bmatrix} f_{xel_{\text{off}}} \\ f_{el_{\text{off}}} \end{bmatrix} \tag{A-5}$$

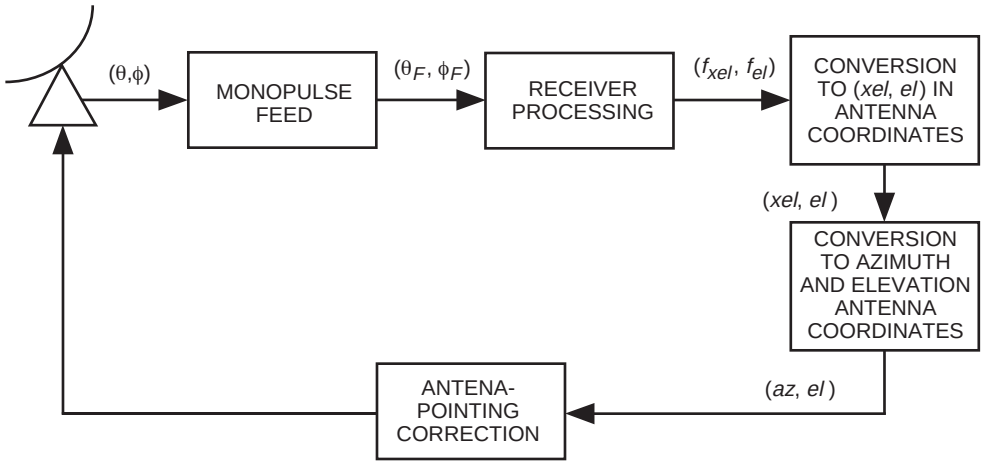

Fig. A-1. The multiple coordinate system referenced in the monopulse implementation.

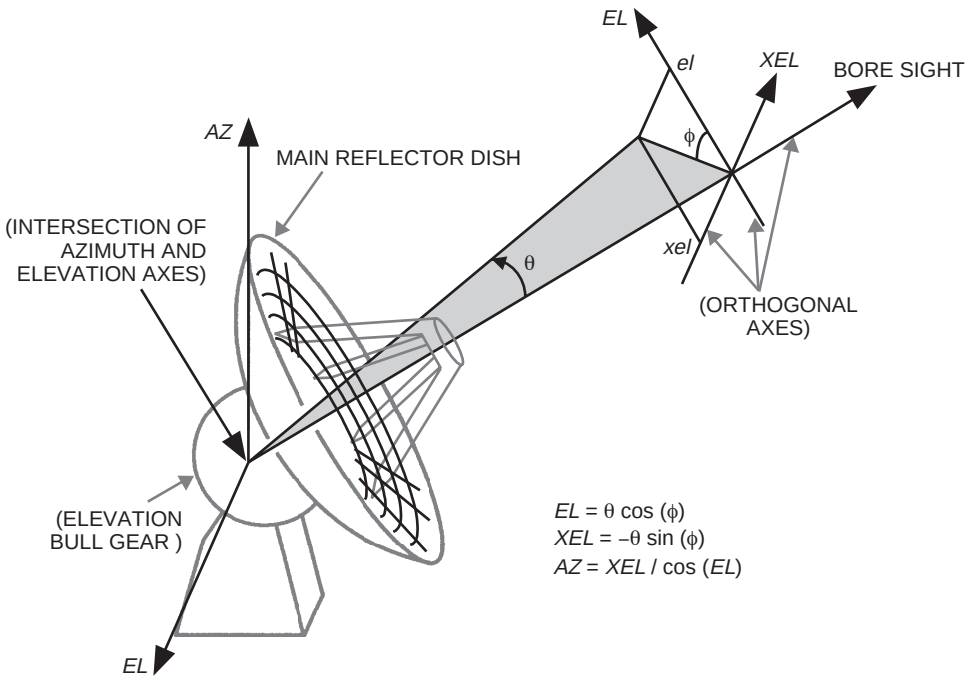

Fig. A-2. The relationship between the multiple coordinate systems within the monopulse implementation.

Appendix B
Antenna and Feed Patterns

Figure B-1 illustrates the ideal antenna–feed patterns. Figure B-1(a) shows the magnitude of the main- and error-channel patterns versus the pointing error, θ_F. For small pointing errors, the main-channel signal is strong and relatively flat, whereas the error-channel signal strength varies proportionally with θ_F. In Fig. B-1(b), the ratio of the magnitudes of the main- and error-channel patterns, defined to be $g(\theta_F, \phi_F)$, is shown as a function of θ_F[$(g(\theta_F, \phi_F)$ is relatively constant as a function of ϕ_F]. Figure B-1(c) shows $\sqrt{g(\theta_F, \phi_F)}$ as a function of θ_F, where

$$\sqrt{g(\theta_F, \phi_F)} \simeq \gamma\theta_F \tag{B-1}$$

where γ is the the slope and is a constant in the ideal case:

$$\frac{d}{d\theta_F}\sqrt{g(\theta_F, \phi_F)} \equiv \gamma(\theta_F, \phi_F)$$

$$= \gamma \tag{B-2}$$

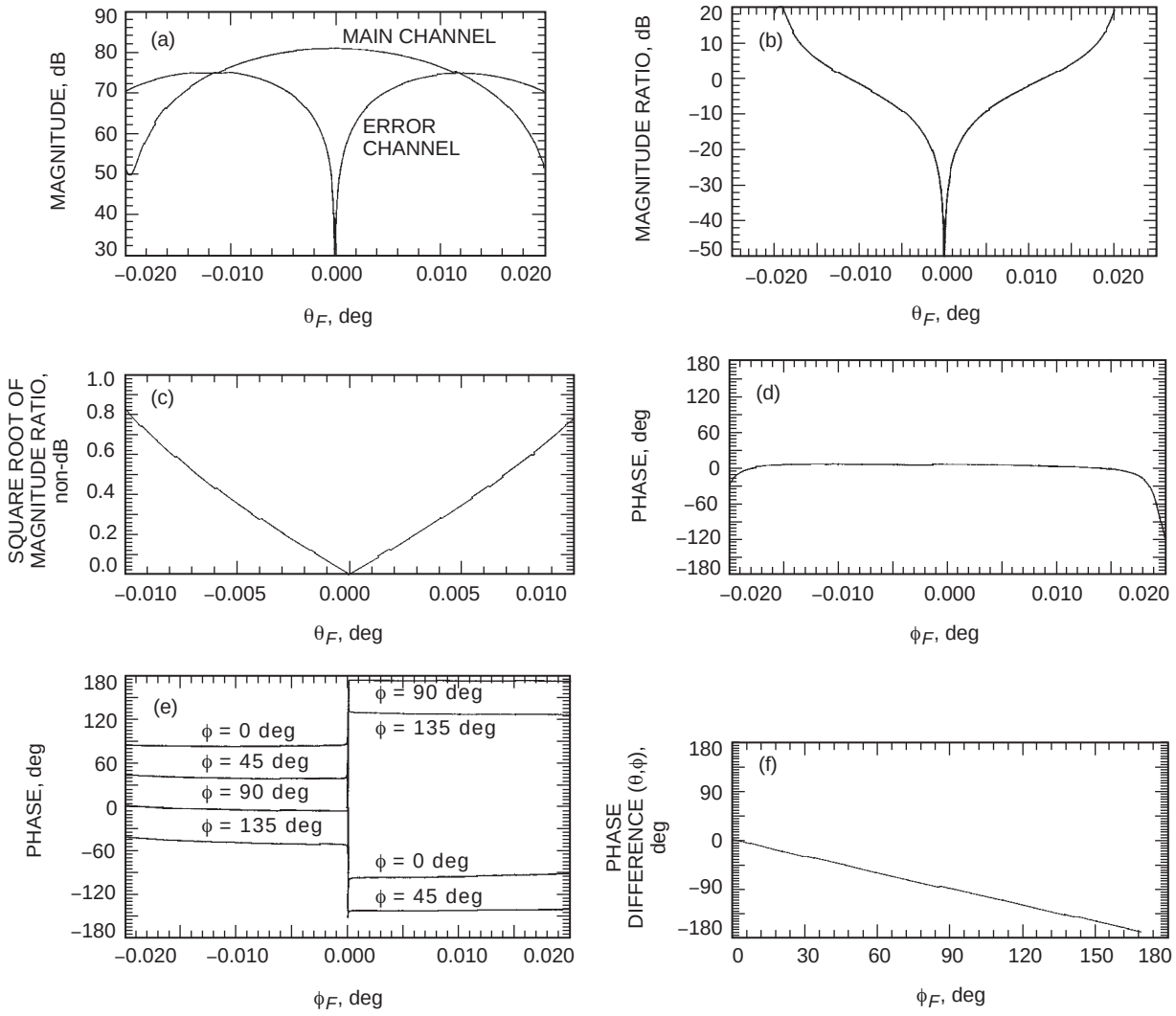

Fig. B-1. Ideal antenna patterns: (a) the magnitude of the main- and error-channel patterns versus θ, (b) *g* (θ,φ), the magnitude of the ratio of the main-channel over the error-channel patterns versus θ (approximately constant as a function of φ), (c)$\sqrt{\ g\ }$(θ,φ) (non-dB), about –10 mdeg < θ < 10 mdeg (ideal case), (d) the phase of the main channel versus θ, (e) the phase of the error channel versus θ, and (f) *h* (θ,φ), the phase difference between the main- and error-channel patterns (approximately constant as a function of θ).

Figures B-1(d) and B-1(e) show the phase of the main- and error-channel signals, respectively. In Fig. B-1(f), the difference between the two channels, defined to be $h(\theta_F, \phi_F)$, is shown as a function of ϕ_F [$h(\theta_F, \phi_F)$ is relatively constant as a function of θ_F], where

$$h(\theta_F, \phi_f) \simeq \phi_F \tag{B-3}$$

The $x_e(t)$ is composed of the signal component proportional to θ_F by the proportionality factor, γ, and a noise component that is independent of γ. Therefore, the larger the value of γ, the larger the signal-to-noise ratio of the received signal. The γ is an intrinsic parameter depending on implementation of the antenna and feed. The implementation goal is to achieve as large a value of γ as possible. For the DSN BWG antennas, $\gamma \simeq 70$ V/V/deg (volts per volt per degree).

I. Null Depth of the Antenna–Feed Pattern

The null depth of the antenna–feed pattern is defined as the ratio of the peak to the valley of $g(\theta_F, \phi_F)$:

$$N[\text{dB}] \equiv 10 \log_{10} \left[\frac{g(\theta_{F,max}, \phi_F)}{g(\theta_{F,min}, \phi_F)} \right] \tag{B-4}$$

In the ideal case, the null depth is infinite.

In the non-ideal case, the null depth, N', is finite and $\sqrt{g'(\theta_F, \phi_F)}$ is non-linear near $\theta_F \simeq 0$. For analysis in this article, the non-ideal null depth was modeled as the ideal null depth degraded by the addition of a constant, representing a constant offset in DC:

$$g'(\theta_F, \phi_F) = \gamma^2 \theta_F^2 + g_{\text{off}}(N') \tag{B-5}$$

where $g_{\text{off}}(N')$ is a constant as a function of N'. A plot of $\sqrt{g'(\theta_F, \phi_F)}$ for a null depth of 15 dB is shown in Fig. B-2. In this case, the slope of$\sqrt{g'(\theta_F, \phi_F)}$ is a function of (θ_F, ϕ_F) rather than a constant:

$$\gamma(\theta_F, \phi_F, N') = \frac{d}{d\theta} \sqrt{g'(\theta_F, \phi_f)} = \frac{a^2 \theta_F}{\sqrt{a^2 \theta_F^2 + g_{\text{off}}(N')}} \tag{B-6}$$

For simulation purposes, the model used was

$$\begin{aligned} g_{\text{off}}(N'(\text{dB})) &= 10^{-[0.5+(N'(\text{dB})/10)]} - g(\theta_{min}, \phi) \\ &\simeq 10^{-[0.5+(N'(\text{dB})/10)]} \end{aligned} \tag{B-7}$$

A reasonable assumption made in the above derivation is

$$g_{\text{off}} \ll g(\theta_{max}, \phi) \times 10^{-5} \tag{B-8}$$

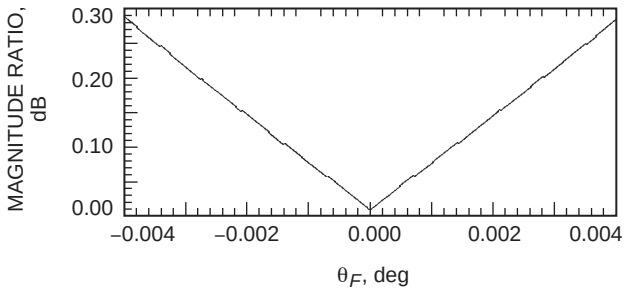

Fig. B-2. $\sqrt{g'(\theta_F, \phi_F)}$ (non-dB), about –10 mdeg < θ< 10 mdeg (non-ideal case); null depth = 15 dB.

II. Degradation to the Monopulse Loop Performance Due to Non-Ideal Antenna–Feed Patterns

Two types of degradation to the monopulse loop occur due to non-ideal antenna–feed patterns. They are limit cycling and bore-sight shift.

A. Limit Cycling

Limit cycling is a degradation in the monopulse loop due to a non-ideal null depth, causing a decrease in slope near $\theta = 0$ and a non-negligible feedback value near $\theta = 0$. To demonstrate this, for $a = 70.6$ V/V/deg (which is the case for DSS 25), $\sqrt{g(\theta_F, \phi_F)}$ is plotted for $N' = 15, 20, 25, 30$, and 35 dB in Fig. B-3. From the figure, it is seen that there exists γ_{limit} such that, for each N', there is a corresponding θ_{limit} below which the loop cannot drive error smaller because of insufficient gain and a non-zero feedback value about $\theta = 0$. Jitter on the monopulse loop due to this inability to reach zero is

$$\sigma^2_{\text{limit}} \simeq \frac{\theta^2_{\text{limit}}}{2} \tag{B-9}$$

For DSS 25,

$$\theta_{\text{limit}}(N') \simeq 0.0014 \times 10^{-[N'(\text{dB})/20]} \tag{B-10}$$

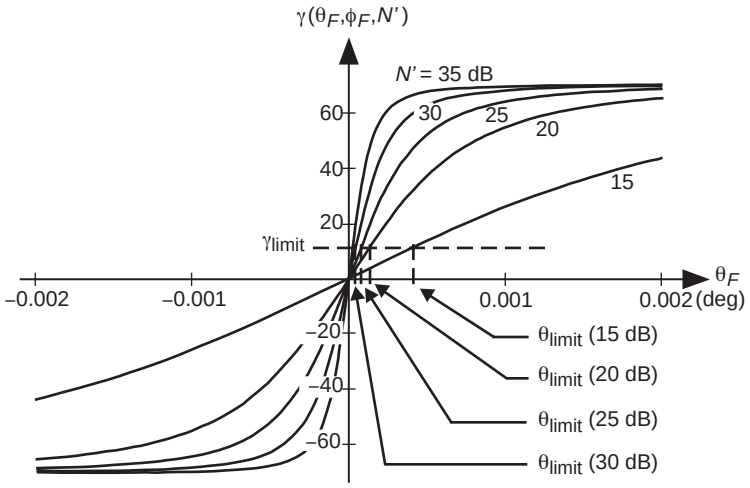

Fig. B-3. γ (θ,φ) versus θ for decreasing values of *N'* dB (null depth).

B. Bore-Sight Shift

A bore-sight shift may be caused by misalignment between the antenna and the feed in implementation, where the RF peak and the null of the antenna pattern are offset by $\theta_{b.s.}$, as shown in Fig. B-4. Such an error is expected to be negligible for the 34-m beam-waveguide antenna implementation, but is discussed here for completeness. This bore-sight shift will move the lock point of the monopulse loop to $\theta_{b.s.}$ away from the RF peak. No significant contribution to the pointing jitter is expected at the lock point.

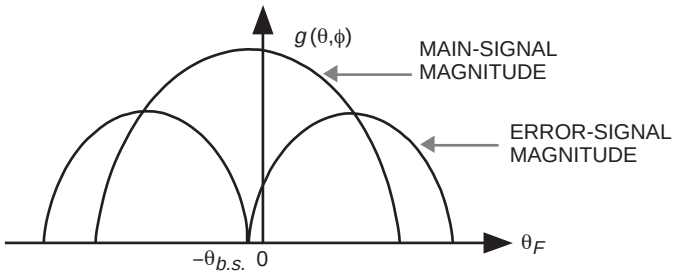

Fig. B-4. Bore-sight shift: offset between the null depth and the RF peak.

Appendix C

Block V Receiver Signal Processing

In this appendix, the Block V receiver (BVR) signal processing, shown in Fig. 2 of the main text, is described. The signals received at the BVR after low-noise amplification are

$$x_{m,\mathrm{LNA}}(t) = \sqrt{2P}\cos(\omega_{c,\mathrm{RF}}t + \theta_c + \Delta D(t)) + n_{m,\mathrm{LNA}}(t) \tag{C-1}$$

$$x_{e,\mathrm{LNA}}(t) = \sqrt{2P}A_1\sqrt{g(\theta_F,\phi_F)}\cos(\omega_{c,\mathrm{RF}}t + \theta_c + \Delta D(t) + \Delta\phi' + h(\theta_F,\phi_F)) + A_1 n_{e,\mathrm{LNA}}(t) \tag{C-2}$$

where

$A_1 =$ the relative amplitude distortion between the main and error channels introduced by independent amplification

$\Delta\phi' =$ the relative phase distortion between the main and error channels introduced by independent amplification

$n_{m,\mathrm{LNA}}(t), n_{e,\mathrm{LNA}}(t) =$ the additive white noise at the output of the LNAs, with a noise spectral density of $N_{o,m}$ and $N_{o,e}$, respectively

These signals are individually downconverted to

$$x_{m,\mathrm{BVR}}(t) = \sqrt{2P}\cos(\omega_{\mathrm{IF}}t + \phi_{\mathrm{IF}} + \Delta D(t)) + n_{m,\mathrm{BVR}}(t) \tag{C-3}$$

$$x_{e,\mathrm{BVR}}(t) = A\sqrt{2P}\sqrt{g(\theta_F,\phi_F)}\cos(\omega_{\mathrm{IF}}t + \theta_{\mathrm{IF}} + \Delta D(t) + h(\theta_F,\phi_F) + \Delta\phi) + A\ n_{e,\mathrm{BVR}}(t) \tag{C-4}$$

where

$(\omega_{\rm IF}, \theta_{\rm IF}) =$ the carrier intermediate frequency (IF) and phase

$n_{m,\rm BVR}(\cdot), n_{e,\rm BVR}(\cdot) =$ the received additive noise at the BVR

$\Delta\phi =$ the relative phase distortion between the main and error channels introduced by independent amplification, downconversion, and signal routing of $x_{m,\rm BVR}(t)$ and $x_{e,\rm BVR}(t)$, respectively

$A =$ the relative amplitude distortion between the main and error channels introduced by independent amplification, downconversion, and signal routing of $x_{m,\rm BVR}(t)$ and $x_{e,\rm BVR}(t)$, respectively

(The distortion in $\Delta\phi$ and A are to be compensated for by calibration.)

At the IF, the signal is digitized and the main signal, $x_{m,\rm BVR}(t)$, is tracked by the standard phase-locked loop. The error signal, $x_{e,\rm BVR}(t)$, is demodulated in phase and in quadrature at the frequency and phase estimated in the main loop. The demodulation signals are

$$\begin{aligned} x_{demod,\cos}(t) &= \cos\left(\hat{\omega}_{\rm IF}t + \hat{\theta}_{\rm IF} + n_{\phi_c}(t) + \Delta\hat{\phi}\right) \\ &\simeq \cos\left(\hat{\omega}_{\rm IF}t + \hat{\theta}_{\rm IF} + \Delta\hat{\phi}\right) \end{aligned} \tag{C-5}$$

and

$$\begin{aligned} x_{demod,\sin}(t) &= \sin\left(\hat{\omega}_{\rm IF}t + \hat{\theta}_{\rm IF} + n_{\phi_c}(t) + \Delta\hat{\phi}\right) \\ &\simeq \sin\left(\hat{\omega}_{\rm IF}t + \hat{\theta}_{\rm IF} + \Delta\hat{\phi}\right) \end{aligned} \tag{C-6}$$

where $n_{\phi_c}(t)$ is the noise in the main-loop carrier tracking, with standard PLL phase jitter [3]:

$$\mathrm{var}[n_{\phi_c}(t)] = \frac{1}{\mathrm{SNR}_{L,\rm main}} = \frac{N_{o,m}B_{L,m}}{P_{c,m}} \tag{C-7}$$

The carrier power at the input of the main carrier tracking loop is $P_{c,m}$, and the bandwidth of the main loop is $B_{L,m}$.

The demodulated signals prior to normalization are

$$\begin{aligned} f'_{xel_{\rm off}}(t) &= [x_{e,\rm BVR}(t)s_{d,\sin}(t)]_{\rm LPF} \\ &\simeq -\frac{1}{2}A\sqrt{2P}\gamma\theta_F \sin(\phi_F + \Delta_{\phi,calib}) + [n_{e,\rm BVR}(t)x_{d,\cos}(t)]_{\rm LPF} \end{aligned} \tag{C-8}$$

where

$$n'_{fxel}(t) \equiv [n_{e,\mathrm{BVR}}(t)x_{d,\cos}(t)]_{\mathrm{LPF}}$$

$[\cdot]_{\mathrm{LPF}} =$ the low-pass filter [in DSN implementation, this is a half-band filter (HBF) followed by an integtate-and-dump filter (IDF)]

$\Delta_{\phi,calib} =$ uncalibrated phase error between the main and error channels

$$= \Delta\phi - \Delta\hat{\phi}$$

and

$$f'_{el_{\mathrm{off}}}(t) = [x_{e,\mathrm{BVR}}(t)s_{d,\cos}(t)]_{\mathrm{LPF}}$$

$$\simeq \frac{1}{2}A\sqrt{2P}\gamma\theta_F\cos(\phi_F + \Delta_{\phi,calib}) + [n_{e,\mathrm{BVR}}(t)x_{d,\sin}(t)]_{\mathrm{LPF}} \tag{C-9}$$

where

$$n'_{fel}(t) \equiv [n_{e,\mathrm{BVR}}(t)x_{d\cos}(t)]_{\mathrm{LPF}} \tag{C-10}$$

The signals are normalized by

$$\hat{K} = \frac{1}{2}\hat{A}\sqrt{2\hat{P}}\hat{\gamma} \tag{C-11}$$

where

$\hat{A} =$ the estimated amplitude calibration

$\sqrt{2\hat{P}} =$ the estimated signal amplitude from the the main signal loop, assuming that $\sqrt{2\hat{P}} + n_{\mathrm{PLL}}(t) \simeq \sqrt{2\hat{P}}$ in the main PLL

$\hat{\gamma} =$ the estimated slope of the S-curve

Normalized estimates of elevation and cross-elevation errors are

$$\hat{f}_{xel_{\mathrm{off}}}(t) = -R_{\mathrm{BVR}}\theta_F\sin(\phi_F + \Delta_{\phi,calib}) + n_{fxel}(t) \tag{C-12}$$

and

$$\hat{f}_{el_{\mathrm{off}}}(t) = R_{\mathrm{BVR}}\theta_F\cos(\phi_F + \Delta_{\phi,calib}) + n_{fel}(t) \tag{C-13}$$

where

$$R_{\mathrm{BVR}} = \frac{A\gamma\sqrt{P}}{\hat{A}\hat{\gamma}\sqrt{\hat{P}}} \tag{C-14}$$

$$n_{fxel}(t) = \frac{n'_{fxel}(t)}{\hat{K}}$$

$$n_{fel}(t) = \frac{n'_{fel}(t)}{\hat{K}}$$

In matrix representation, the output of the BVR is

$$\begin{aligned}\begin{bmatrix} \hat{f}_{xel_{\text{off}}}(t) \\ \hat{f}_{el_{\text{off}}}(t) \end{bmatrix} &= R_{\text{BVR}}(\theta,\phi) \begin{bmatrix} \cos(\phi_{\Delta,\text{BVR}} & -\sin(\phi_{\Delta,\text{BVR}}) \\ \sin(\phi_{\Delta,\text{BVR}} & \cos(\phi_{\Delta,\text{BVR}}) \end{bmatrix} \begin{bmatrix} -\theta_F \cos(\phi_F) \\ \theta_F \sin(\phi_F) \end{bmatrix} + \begin{bmatrix} n_{fxel}(t) \\ n_{fel}(t) \end{bmatrix} \\ &= R_{\text{BVR}} \begin{bmatrix} \cos(\Delta_{\phi,calib} & -\sin(\Delta_{\phi,calib}) \\ \sin(\Delta_{\phi,calib} & \cos(\Delta_{\phi,calib}) \end{bmatrix} \begin{bmatrix} xel_{\text{off}} \\ el_{\text{off}} \end{bmatrix} + \begin{bmatrix} n_{fxel}(t) \\ n_{fel}(t) \end{bmatrix} \end{aligned} \tag{C-15}$$

where $xel_{\text{off}} = -\theta_F \sin(\phi_F)$ (Appendix A) and $el_{\text{off}} = \theta_F \cos(\phi_F)$ (Appendix A).

Appendix D
System Noise Analysis

Pointing-error jitter contribution due to the additive white noise at the input of the monopulse system is evaluated here as $\sigma^2_{\text{sys noise}}$, which is the same in the cross-elevation and elevation axes because their equivalent models are the same. The system-noise jitter contribution is

$$\begin{aligned}\sigma^2_{\text{sys noise}} &= N_{0,\text{BVR out}} B'_{L,m} \\ &= \frac{1}{\gamma^2} R_{\text{BVR}} \left(\frac{A}{\hat{A}}\right)^2 \times \frac{N_{o,e} B_{L,m}}{P_{c,m}} \end{aligned} \tag{D-1}$$

where

$$
\begin{aligned}
B'_{L,m} &= \text{the equivalent bandwidth of the monopulse loop} \\
&= B_{L,m} \times R_{\mathrm{BVR}} \\
N_{0,\mathrm{BVR\ out}} &= \text{the spectral density of additive noise after BVR processing} \\
&= 2T_{upd} \times \mathrm{Var}\left[n_{f,el}(\cdot)\right] = 2T_{upd} \times \mathrm{Var}\left[n_{f,xel}(\cdot)\right] \\
\mathrm{Var}\left[n_{fel}(t)\right] &= \mathrm{Var}\left[n_{fxel}(t)\right] \\
&= \frac{1}{2}\left(\frac{A}{\hat{K}}\right)^2 \mathrm{Var}\left[n_{e,\mathrm{LNA}}(\cdot)\right] \\
&= \frac{1}{2}A^2\frac{N_{0,e}}{2T_s}\left(\frac{1}{\frac{1}{2}\hat{A}\sqrt{2\hat{P}}\hat{\gamma}}\right)^2 \frac{f_{upd}}{f_s} \\
\mathrm{Var}\left[n_{e,\mathrm{LNA}}(\cdot)\right] &\equiv \frac{N_{0,e}}{2T_s} \\
f_s &= \frac{1}{T_s} = \text{the sampling rate of the receiver} \\
f_{ups} &= \frac{1}{T_{upd}} = \text{the sampling rate of the monopulse loop}
\end{aligned}
$$